

Article

Hierarchical Porosity and Surface Oxygenation of Carbon-Based Cathodes Enhances Discharge Capacity and Decreases Discharge Overpotential of Potassium–Oxygen Batteries

Shikha Singh, Jannis Küpper, Ahed Abouserie , Gianluca Dalfollo , Michael Noyong  and Ulrich Simon *

Institute of Inorganic Chemistry, RWTH Aachen University, 52072 Aachen, Germany; shikha.singh@ac.rwth-aachen.de (S.S.); jannis.nicolas.kuepper@rwth-aachen.de (J.K.); ahed.abouserie@ac.rwth-aachen.de (A.A.); gianluca.dalfollo@ac.rwth-aachen.de (G.D.); michael.noyong@ac.rwth-aachen.de (M.N.)

* Correspondence: ulrich.simon@ac.rwth-aachen.de; Tel.: +49-241-80-94644

Abstract: Potassium–oxygen batteries (KOBs) are a promising energy storage technology with high theoretical energy density, low overpotential and a long cycle life. The cathode microstructure plays a significant role in the electrochemical performance of KOB. In this article, hierarchical porosity was introduced to commercially available carbon paper cathodes by thermal pretreatment in air at different pretreatment times. This pretreatment modifies the properties, such as surface area, defects, oxygen functional groups, etc. The discharge performance was determined at three different current densities, i.e., 0.1 mA/cm², 0.5 mA/cm², and 1.0 mA/cm². It has been found that an increase in specific surface area with the introduction of micropores and mesopores is beneficial for the improvement in the discharge capacity by enabling homogeneous discharge product, KO₂ distribution and high degrees of pore filling over the volume of the cathode. A reduction in the discharge overpotentials was observed, which is attributed to the introduction of oxygenic functional groups and defects. Samples treated for the longest pretreatment time of 24 h showed the highest discharge capacity of 5 mAh/cm² and lowest discharge overpotential of 0.03 V.

Keywords: carbon paper; thermal pretreatment; defects; oxygen functional groups; discharge capacity



Citation: Singh, S.; Küpper, J.; Abouserie, A.; Dalfollo, G.; Noyong, M.; Simon, U. Hierarchical Porosity and Surface Oxygenation of Carbon-Based Cathodes Enhances Discharge Capacity and Decreases Discharge Overpotential of Potassium–Oxygen Batteries. *Batteries* **2024**, *10*, 192. <https://doi.org/10.3390/batteries10060192>

Academic Editor: Jun Yan

Received: 23 April 2024

Revised: 17 May 2024

Accepted: 29 May 2024

Published: 31 May 2024



Copyright: © 2024 by the authors. Licensee MDPI, Basel, Switzerland. This article is an open access article distributed under the terms and conditions of the Creative Commons Attribution (CC BY) license (<https://creativecommons.org/licenses/by/4.0/>).

1. Introduction

The storage and effective utilization of intermittently harvested energy electricity continue to pose challenges. Although lithium-ion batteries (LIBs) dominate the energy storage market for portable electronic devices, their energy density, earth crustal abundance, and cost still challenge their suitability for next-generation large-scale energy storage applications. Among the alternatives, metal–oxygen batteries have attracted considerable attention, especially the lithium–oxygen battery (LOB) due to its high theoretical energy density of 3505 Wh/kg and potentially lower cost [1–3]. However, the practical capacities of LOBs have not reached its theoretical predictions yet. The main causes can be found in the complex cell chemistry of the LOB, which gives rise to large charging overpotential, low energy efficiency, limited rechargeability, and severe electrolyte/electrode decomposition [4,5]. In particular, LOBs suffer from cell degradation caused by reactive singlet oxygen (¹O₂) formed during all stages of cycling [6,7]. In contrast, in the potassium oxygen battery (KOB) the main discharge product is potassium superoxide (KO₂), which allows for recharging with negligible ¹O₂ formation [8–13].

However, KOB is not yet intensely studied, which could be attributed to its lower specific energy in comparison to other MOBs [12]. Additionally, O₂ crossover from the cathode compartment to the K-metal anode leads to permanent self-discharge, due to which a limited cycle life is observed [14].

In order to mitigate self-discharge and dendrite formation [14–19], an “organic” KOB cell design was developed, comprising a liquid anode consisting of a potassium biphenyl complex (KBp) in 1,2-dimethoxyethane (DME). This new anode type offers low interfacial resistances with a $K-\beta''$ alumina solid state electrolyte (KBA) acting as an O_2 -impermeable separator [20]. Although the standard cell potential of $E_{(KBp/O_2)} = 2.18$ V is lowered compared to a K-metal anode (2.48 V), by employing carbon paper as the cathode, cycling at a limited areal discharge capacity (Q) of 0.25 mAh/cm 2 for 3000 cycles with an average current efficiency of 98.5% has been achieved.

In order to develop KOBs to a higher technology readiness level, this remarkable rechargeability needs to be further evolved towards significantly higher discharge capacities. Recently, we were able to show that the surface functionalization of a commercial carbon paper cathode with hydrophobic PTFE enhances the discharge capacity by improving the mass transport [21]. Further improvements were achieved by an O_2 partial pressure increase [22], and by means of a very recently introduced physical–mathematical model, which describes the influence of cathode porosity and the microstructure on the discharge performance. We predicted that increasing the cathode porosity and volumetric surface area is further supportive for the discharge performance [23]. Through this, it became evident that a combination of micropores and mesopores is particularly supportive to avoid oxygen transport limitations in inner cathode regions [23]. Therefore, a hierarchical pore design of cathode material is anticipated to be most promising. In our previous work, we utilized commercial carbon materials with relatively low porosity. In view of the arguments given above, commercial carbon materials can be structurally optimized to improve the performance of KOB by introducing hierarchical surface porosity as well as by modifying the surface properties to enhance the electrochemical performance [24].

In this work, we developed carbon cathode materials with hierarchical porosity by thermal treatment of the commercial carbon paper in air at selected temperature for varied pretreatment times. The pretreatment causes partial thermal oxidation of the carbon fibers and results in surface oxygenation and an increase in the available and physical surface area [25,26]. In a systematic study, we investigated the discharge performance of the pristine carbon paper cathode and all pretreated cathode samples in an organic KOB to analyze how the change in the properties of carbon paper such as the introduction of oxygen functional groups, defects, surface area, etc., affects the discharge performance.

2. Materials and Methods

2.1. Thermal Oxidation of Carbon Paper

Carbon paper, H23, (Freudentenberg, Weinheim, Germany), denoted as CP was punched into circular discs ($m = 14.6$ mg \pm 0.1 mg, $\varnothing = 14$ mm, $T = 0.211$ mm) and then, they were oxidized under air in a muffle furnace (Nabertherm muffle furnace, Nabertherm GmbH, Lilienthal, Germany) at 450 °C for varying pretreatment times of $t_{pt} = 4$ h, 12 h, and 24 h, denoted as CP_4 h, CP_12 h, and CP_24 h, respectively. CP treated for more than 24 h lost a significant amount of their mass and were too fragile. For the pretreatment, the CP discs were placed on aluminum foil to avoid any contamination, and care was taken to prevent the carbon paper discs from overlapping. The CP discs were kept in the oven at room temperature, and the temperature was ramped to the set-point, i.e., 450 °C at 10 °C/min. Then, the oven temperature was held at this temperature for the specified time t_{pt} . After the treatment, the samples were allowed to cool to the room temperature in the oven and were thereafter stored in glass vials.

2.2. Characterization

Electron microscopy was conducted by means of a scanning electron microscope (SEM) at an accelerating voltage of 10 kV with a LEO Supra35VP (Carl Zeiss AG, Oberkochen, Germany) SEM device with an integrated energy-dispersive X-ray spectroscopy (EDS) INCA Energy 200 detector (Oxford Instruments, Abingdon, UK), a JSM-IT800HL SEM (JEOL, Tokyo, Japan) with integrated EDS Octane Elect from EDAX (AMETEK, Weiterstadt,

Germany), and a transmission electron microscope (TEM) using ZEISS LIBRA 200 FE operating at 200 kV. Raman spectroscopy was performed using a Renishaw Virsa/InLux (Renishaw, Aberdeen, UK) with a laser wavelength of 532 nm. X-ray photoelectron spectroscopy (XPS) was performed using an AXIS Supra instrument (Kratos Analytical Ltd., Manchester, UK) with a monochromatized Al K α X-ray source, and the base pressure was $<5.0 \times 10^{-6}$ Pa. The analysis of the spectra was performed in the CasaXPS software package (Casa Software Ltd., Teignmouth, UK). Nitrogen adsorption/desorption measurements for the Brunauer–Emmett–Teller (BET) surface area determination were obtained using an Autosorb-iQ analyzer (Autosorb-iQ, Quantachrome, Boynton Beach, FL, USA) with liquid nitrogen at 77 k. All the samples were degassed at 120 °C for 12 h under high vacuum to remove any adsorbed species prior to measurement. The mass loss of the samples was determined by weighing the samples before and after the thermal pretreatment using XS205 Mettler Toledo balance. Contact angle measurement of the samples was performed to compare the wettability. Measurements were taken in ambient air at room temperature. Specifically, a 2 μ L solvent drop of either deionized (DI) water or DMSO was placed on the porous cathode surface, and an image of the droplet on the surface was captured immediately. The contact angle measurement was estimated manually using ImageJ software (Version 1.49).

2.3. Battery Cell Assembly

All the solvents were dried over 3 Å molecular sieves for at least two weeks before use. Moisture contents were assessed by Karl–Fischer Titration (KFT) to be <20 ppm. Biphenyl (Bp, 99%, Sigma-Aldrich, St. Louis, MO, USA) was vacuum-dried at RT for 2 days and transferred to an argon-filled glovebox ($H_2O < 0.1$ ppm, $O_2 < 0.1$ ppm) without any air exposure. KPF_6 (99.5%, Sigma-Aldrich) was vacuum-dried at 110 °C overnight and transferred to a glovebox without any air exposure. K metal (99.5%, Sigma-Aldrich) was used as received. The cell assembly process was performed in argon-filled glovebox. Battery cells were based on ECC-Air cells (EL-Cell, Hamburg, Germany) with a homemade inlay [21]. The cell and inlay components were dried at 105 °C overnight and transferred to the glovebox while hot. Cell assembly was carried out in the glovebox. Cu foam ($\varnothing = 16$ mm, $T = 2.0$ mm, >99%, Alfa Aesar, Ward Hill, MA, USA) and a grade GF/B filter ($m = 22.0$ mg ± 0.1 mg, $\varnothing = 14$ mm, Whatman, Little Chalfont, UK) were inserted into the anode compartment of the inlay. Then, 200 μ L of 3.0 M KBp in 1,2-dimethoxy ethane (DME, 99.5%, anhydrous, Sigma-Aldrich) was added. The average thickness of anode was 0.75 mm and diameter was 14 mm, resulting in an area of 1.54 cm 2 . K- β'' alumina disks (KBA, $\varnothing = 20$ mm, $T = 1.0$ mm) was placed on top. The upper polyether ether ketone (PEEK) inlay component was put into the place and the anode compartment was sealed with PEEK clamps. Grade GF/A ($m = 10.2$ mg ± 0.1 mg, $\varnothing = 16$ mm, Whatman, UK) was inserted into the cathode compartment. Then, 60 μ L of 0.5 M KPF_6 in dimethyl sulfoxide electrolyte (DMSO, 99.9%, anhydrous, Sigma-Aldrich) was added. Sample was inserted, and a perforated stainless-steel current collector disk was placed on top followed by a copper spring for compression. The inlay was transferred to the ECC-Std cell housing and the cell was sealed with the cell clamp.

2.4. Electrochemical Measurements

Fully assembled cells were removed from the glovebox, transported to the test bench and connected to the O_2 supply. Cells were purged under rapid O_2 flow for 2 min. Battery tests were performed with a CTS battery tester (Basytec, Asselfingen, Germany). A 75 min resting step at open-circuit potential was performed prior to battery testing. Discharge currents were normalized to the nominal surface area of electrodes ($A = 1.54$ cm 2). The cutoff cell voltage was 1.50 V. Electrochemical impedance spectroscopy (EIS) measurements were conducted using a potentiostat (BioLogic SP-200, BioLogic, Seyssinet-Pariset, France). EIS spectra were recorded at open-circuit voltage with 5 mV excitation amplitude and the

frequency scan range was from 100 KHz to 0.010 Hz, with 9 points per decade. EIS spectra were analyzed by Bio-Logic EC lab software (Version 11.40).

2.5. Analysis Methods Post Discharge

Samples were prepared by removing cathodes from cells in the glovebox and rinsing them thoroughly with DME in order to remove any residual electrolyte. SEM was performed as described in Section 2.2. Cross-sections of cathodes were obtained by cutting the cathode using a scalpel.

3. Results and Discussion

3.1. Thermal Oxidation of Carbon Paper

3.1.1. Analysis of Cathode Structure and Surface Properties

Figure 1A shows the scheme of the thermal oxidation of pristine carbon paper, which consists of interwoven fibers, which show initially a smooth surface. By thermal treatment (4 h, 12 h and 24 h) their surface is intended to be modified in terms of roughness and oxygen containing functional groups. The pristine and modified carbon paper fibers were analyzed by SEM. The images were obtained to qualitatively assess the impact of thermal pretreatment on the microstructure of cathode. At moderate magnifications, all cathode samples appear similar with respect to their microstructure (Figure S1). However, Figure 1D shows that at higher magnification, the pristine CP exhibited a smooth fiber surface. In contrast, the fiber surfaces of CP_4 h, CP_12 h, and CP_24 h became texturized with increase in pretreatment time, indicating that the surface of cathode samples has been modified after thermal pretreatment. EDS mapping was performed for all the cathode samples to locate oxygen on the carbon fiber surface. Even EDS is not ideally suited here for a quantitative determination of the oxygen amount, the oxygen intensities under identical measuring parameters can be compared semi-quantitatively. The oxygen maps of CP, CP_4 h, CP_12 h and CP_24 h are shown in Figure 1C and reveal almost no intensity for the untreated CP up to a max intensity for the longest pretreatment time, i.e., CP_24 h. The full set of EDS analysis is given in Figure S2. Supplementing TEM analysis shows that the CP has a smooth fringe while the CP_24 h became rough (Figure S3).

To determine the mass loss, samples were weighed before and after pretreatment. There was no noticeable mass loss for CP_4 h, while mass loss of 3 to 5% and 10 to 15% was observed for CP_12 h and CP_24 h, respectively. To assess the wettability of the cathode samples, contact angle measurements were performed with droplets of DI water and DMSO. The pristine CP is observed to be hydrophobic with an external contact angle of $\sim 109^\circ$ C for DI water. In contrast, CP_4 h, CP_12 h and CP_24 h immediately imbibe the water droplet upon contact, implying that an introduction of oxygen functional groups on the fiber surface induces wetting (Figure S4). All pristine and pretreated cathode samples immediately imbibe the DMSO droplets as well, evincing good wettability for the polar electrolyte solvent, DMSO.

Carbon material is widely characterized by Raman spectroscopy [27]. The most interesting Raman bands for sp^2 hybridized carbon materials and their composites are two signals at $\sim 1350\text{ cm}^{-1}$ and $\sim 1580\text{ cm}^{-1}$, which are the disordered (D) and graphitic (G) modes of carbon, respectively. Structural changes [28] as defect densities can be monitored by their intensity ratio I_D/I_G . Here, Raman spectra show two bands at $\sim 1351\text{ cm}^{-1}$ and $\sim 1570\text{ cm}^{-1}$ for all the cathode samples (Figure S5). Intensity ratios I_D/I_G for CP, CP_4 h, CP_12 h and CP_24 h were found to be 0.92, 0.99, 1.05, and 1.07, respectively, indicating an increase in surface disorder and defects of the carbon structure with increasing pretreatment time.

The chemical surface composition of the cathode samples was also investigated by means of XPS. Figure 2A shows the wide scan XPS survey spectra of CP, CP_4 h, CP_12 h, and CP_24 h, which indicate the presence of carbon and oxygen at approximately 285.0 eV and 533.0 eV, respectively [29]. The O 1s peak intensity at 533.0 eV was lowest for the CP and it gets more pronounced with thermal treatment time, indicating the thermal

oxidation process introduced more oxygen-containing functional groups on the surface of the carbon paper. For further analysis, C 1s spectra and O 1s spectra were deconvoluted (Figures S6 and S7). It can be seen that the C 1s spectrum of CP shows deconvoluted peaks for graphitic carbon (~284.6 eV), defective carbon (~285.3 eV), C–O (~286.7 eV), and O–C=O (~289.7 eV) while CP_4 h, CP_12 h, and CP_24 h show deconvoluted peaks for graphitic carbon (~284.6 eV), defective carbon (~285.3 eV), C=O (~287.4 eV), and O–C=O (~290.2 eV) [25,26,30–32]. This high-resolution C 1s spectrum shows a decrease in graphitic carbon with an increase in defective carbon with increasing pretreatment time. This effect is more pronounced from CP to CP_4 h. The O 1s spectrum of CP reveals deconvoluted peaks for C–O (~532.2 eV), O–C=O (~533.5 eV) and chemisorbed oxygen or perhaps some water (534.7 eV), while CP_4 h, CP_12 h, and CP_24 h shows peaks for C=O (~531.2 eV), O–C=O (~533.eV), adsorbed water (~535.5 eV) and adsorbed CO₂ (~536.9 eV) [25,26,33,34]. The content of the O–C=O groups increases with the pretreatment time and the most significant increase is observed from CP to CP_4 h.

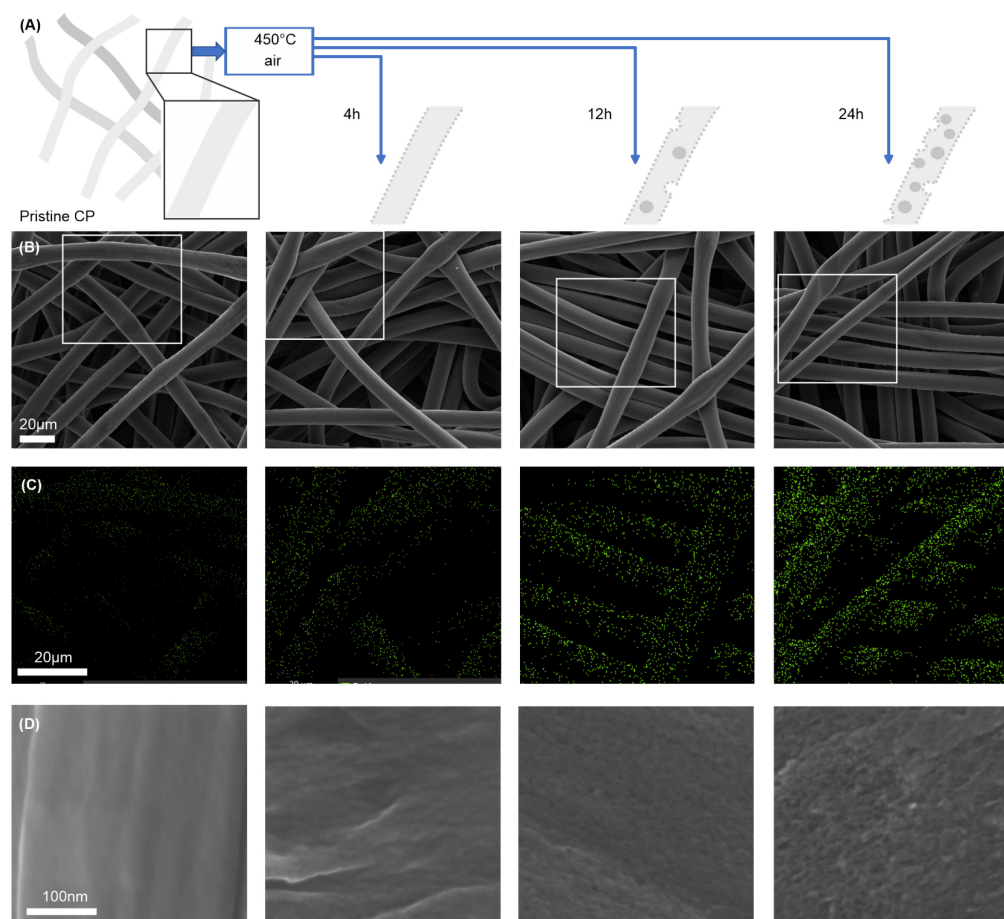


Figure 1. (A) Schematic drawing of the thermal oxidation of carbon paper. Pristine carbon paper consists of interwoven fibers, which show initially a smooth surface. By thermal treatment (4 h, 12 h and 24 h), their surface was intended to be modified in terms of roughness and oxygen-containing functional groups. (B) SEM overview images of CP (from left to right: pristine, 4 h, 12 h and 24 h treatment) with boxes, where (C) their respective EDS mappings of oxygen (green dots) were taken. (D) Higher magnified SEM images. Scale bars apply to each row. Full mappings and sum spectra of the investigated areas can be found in Figure S2.

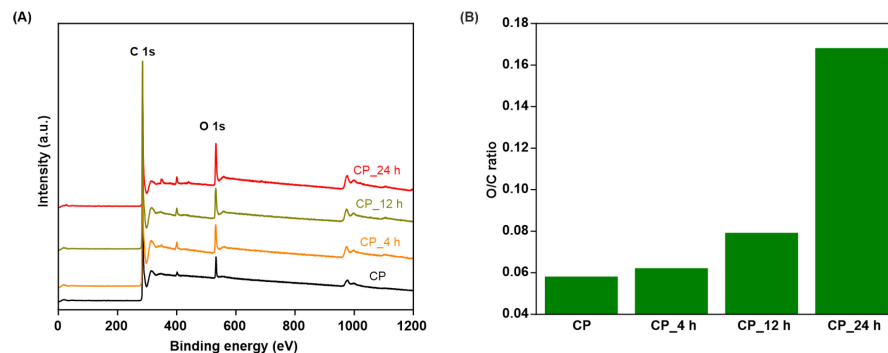


Figure 2. (A) Full survey spectra of CP, CP_4 h, CP_12 h, and CP_24 h. (B) O/C ratio calculated from integrals of O 1s and C 1s peaks of CP and CP_4 h, CP_12 h and CP_24 h.

To evaluate the introduction of oxygen-containing functional groups, the ratio of O/C was calculated from the integrals of O 1s and C 1s peaks. Figure 2B shows the O/C ratio for all samples. It is evident that the O/C ratio increases with the pretreatment time indicating more surface coverage of the oxygen containing functional groups with values of 0.058, 0.062, 0.079 and 0.168, respectively. However, the O/C ratio does not show a significant increase for CP_4 h, but successive increase for CP_12 h and CP_24 h.

3.1.2. Analysis of Surface Area

Table 1 shows the micropore area, external surface area and specific surface area of all the cathode samples. It can be seen that CP and CP_4 h have a low specific surface area of $0.33 \text{ m}^2/\text{g}$ and $1.2 \text{ m}^2/\text{g}$, respectively, and the values are too low for the accurate quantification of micropore area and external surface area. The specific surface area of CP_12 h was nearly 29 times that of CP_4 h and CP_24 h is nearly threefold that of CP_12 h. From the pore size distributions of CP_12 h and CP_24 h shown in Figure 3, micropores presence can be observed in CP_12 h while higher concentration of micropores and very less concentration of mesopores at an average size of around 3 nm and 6 nm can be seen for CP_24 h.

Table 1. Summary of the micropore area, external surface area and specific surface area of all cathode samples.

Cathode Sample	Micropore Area (m^2/g)	External Surface Area (m^2/g)	Specific Surface Area (m^2/g)
CP	-	-	0.33
CP_4 h	-	-	1.2
CP_12 h	26	3	29
CP_24 h	75.7	18.2	90

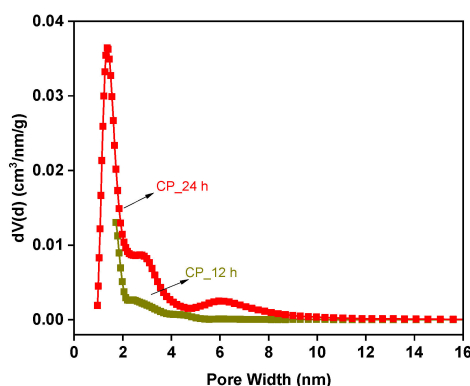


Figure 3. Pore size distribution of CP_12 h and CP_24 h.

3.2. Electrochemical Measurements

Discharge testing was conducted for all the cathode samples at three different current densities, J values of 0.1 mA/cm^2 , 0.5 mA/cm^2 and 1.0 mA/cm^2 . Discharge profiles of all the cathode samples are shown in Figure 4. For all cathodes, only one plateau is visible at all tested J and a second voltage plateau is not visible, which could indicate the unintended formation of K_2O_2 [22]. In our previous studies, KO_2 was already identified as the discharge product by means of X-ray diffraction and Raman spectroscopy [21]. Typically, the discharge overpotential, η_{dis} , increases with an increase in J , while Q decreases.

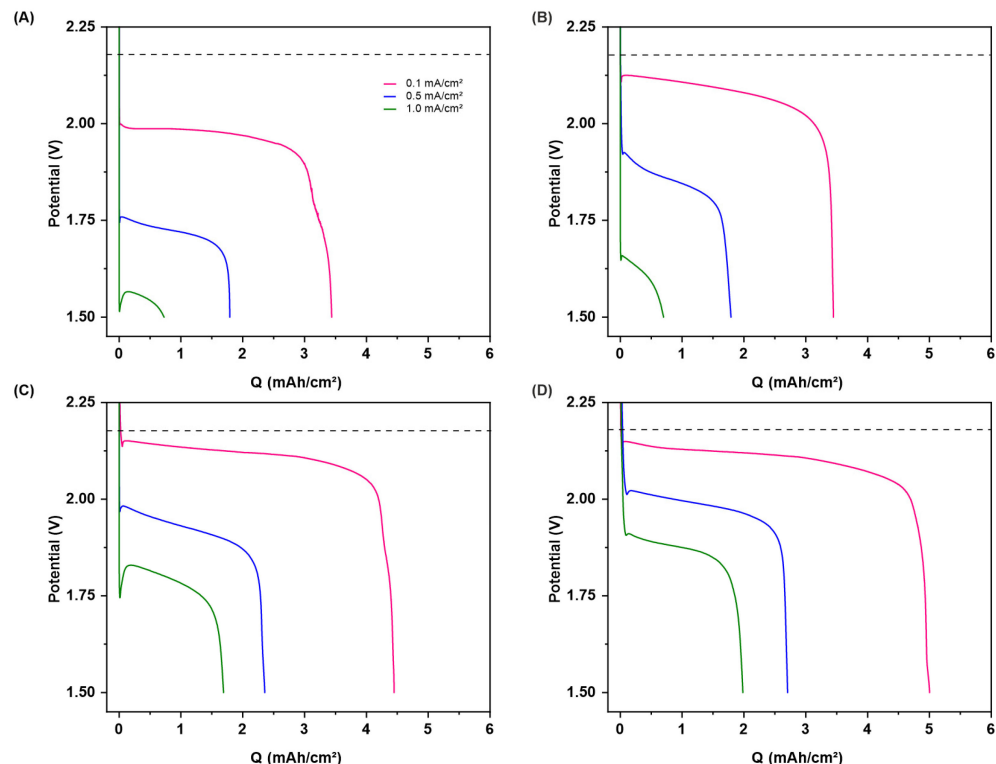


Figure 4. Discharge profiles for KOB cells with cathode samples (A) CP, (B) CP_4 h, (C) CP_12 h, and (D) CP_24 h for $J = 0.1 \text{ mA/cm}^2$ (pink), $J = 0.5 \text{ mA/cm}^2$ (blue), and $J = 1.0 \text{ mA/cm}^2$ (green). The dashed black line indicated the open circuit potential $E^\circ(\text{KBp}/\text{O}_2) = 2.18 \text{ V}$.

The specific double-layer capacitance, C_{sp} , of an electrode in contact with electrolyte was investigated by means of electrochemical impedance spectroscopy via a previously reported method [35]. C_{sp} is known to be directly proportional to the area of solid–liquid interface [36]. Figure 5 shows the bar plot of C_{sp} and of specific surface area (cf. Table 1) of all the cathode samples. The corresponding Bode plots of all the cathode samples can be found in Figure S8. There is a significant increase in C_{sp} from CP_4 h to CP_12 h, indicating the maximum available active surface area, with an increase of 29-fold in specific surface area. However, the C_{sp} increase gets less pronounced from CP_12 h to CP_24 h as the specific surface area only increases to 3-fold.

Figure 6A shows the Q with the specific surface area of the cathode samples CP, CP_4 h, CP_12 h and CP_24 h (left to right). CP and CP_4 h shows lowest Q with almost similar values at all the three J which could be due to the lower specific surface area of both samples. It can be observed that CP_12 h shows a tremendous increase in Q of nearly 28% to 140% at 0.1 mA/cm^2 and 1.0 mA/cm^2 than that of CP_4 h, being consistent with the described increase in specific surface area and the introduction of microporosity. The latter is deemed to be beneficial for the transport of oxygen [37] and ion diffusion. These results show that the pore structure with micropores (on the surface of carbon fibers) and macropores (already present as free space between fibers) are supportive for catalytic activity for oxygen

reduction reaction. CP_24 h shows a further, but less pronounced increase of nearly 11% to 17% of Q at 0.1 mA/cm² and 1.0 mA/cm² than that of CP_12 h, with a three-fold increase in specific surface area due to the introduction of a higher concentration of micropores and an additional small amount of mesopores at around 3 nm and 6 nm. As discussed in the literature, mesopores can be assumed to provide additional accommodation sites for the discharge product and enables better gas diffusion [38]. Furthermore, hierarchical pores with numerous micropores connected to open macropores and mesopores were shown to facilitate oxygen and rapid ion diffusion to the surface of the cathode [39]. In line with these findings, the increase in specific surface area found in our experiments can improve the discharge capacity of the cathode due to hierarchical porosity.

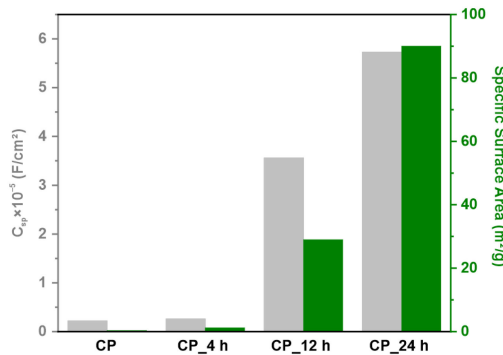


Figure 5. Bar plot of the specific double-layer capacitance C_{sp} (grey bars, left y-axis) and the specific surface area (green, right y-axis) of the samples CP, CP_4 h, CP_12 h and CP_24 h.

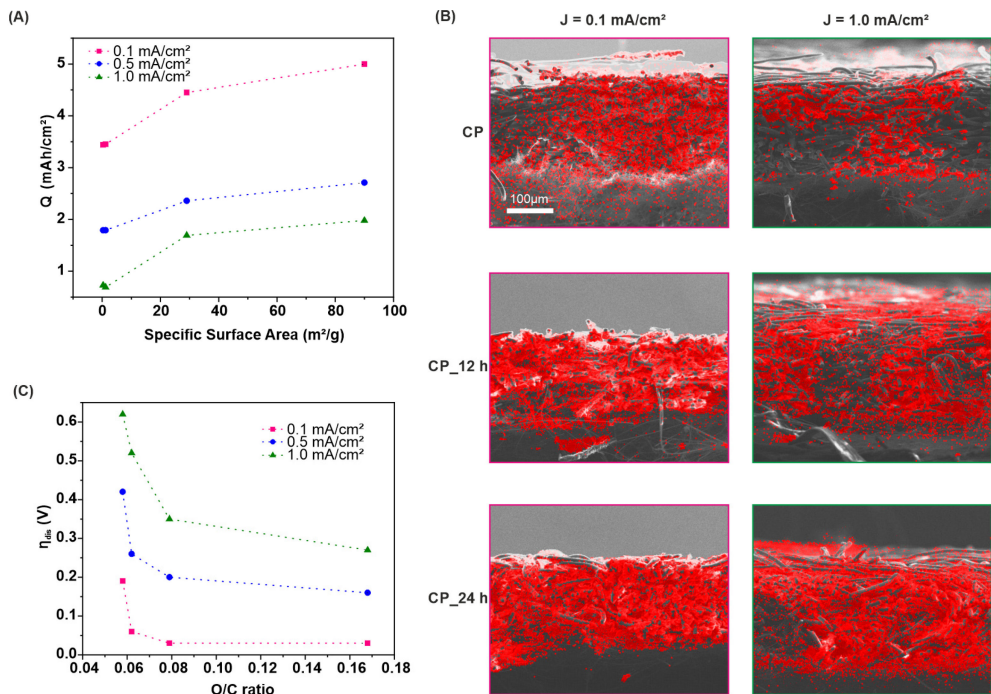


Figure 6. (A) Discharge capacity, Q plotted versus the specific surface area determined by BET for CP, CP_4 h, CP_12 h and CP_24 h at $J = 0.1$ mA/cm² (pink), $J = 0.5$ mA/cm² (blue), and $J = 1.0$ mA/cm² (green). Dashed lines serve as guidance for the eye. (B) Cross-sectional SEM images of cathode samples with overlaid K_K EDS maps (red dots). The rows show the micrographs for CP, CP_12 h and CP_24 h after discharge at $J = 0.1$ mA/cm² (pink framed) and $J = 1.0$ mA/cm² (green framed). (C) Discharge overpotentials, η_{dis} plotted versus the O/C-ratios of CP, CP_4 h, CP_12 h and CP_24 h at $J = 0.1$ mA/cm² (pink), $J = 0.5$ mA/cm² (blue), and $J = 1.0$ mA/cm² (green). Dashed lines serve as guidance for the eye. The values of Q and η_{dis} are given in Table S1.

Figure 6B shows EDS K maps of the KO₂ (indicated by red dots) distribution along the cross sections of CP, CP_12 h and CP_24 h at J of 0.1 mA/cm² and 1.0 mA/cm². It can be observed that the discharge at low J of 0.1 mA/cm² leads to a rather homogenous distribution of KO₂ along the CP cathode. In contrast, discharge at a high J of 1.0 mA/cm² results in the KO₂ formation in the regions close to the O₂ supply, while very little KO₂ is observed near the regions close to electrolyte reservoir. This is consistent with oxygen transport limitations at high J [21]. The discharge of CP_12 h at low J of 0.1 mA/cm² results in higher pore filling, with dense KO₂ growth along the entire cathode than the CP at J of 0.1 mA/cm². A discharge of CP_12 h at high J of 1.0 mA/cm² results in more KO₂ formation than that of CP at same J. However, there are still some unoccupied cathode voids that can be observed. CP_24 h after discharge at 0.1 mA/cm² shows that the entire cathode is fully occupied by KO₂ and almost no free macropore voids are visible, while at higher J of 1.0 mA/cm², there is maximum utilization of the cathode free space by KO₂ formation across the cathode structure compared to CP and CP_12 h at J of 1.0 mA/cm². So, the improvement in Q from CP to CP_12 h can be attributed to the introduction of micropores on the surface of carbon fibers while a little improvement in Q from CP_12 h to CP_24 h can be due to the increase in micropores and an additionally implemented amount of mesopores which leads more filling by the KO₂ across the cathode. So, the thermal treatment of carbon paper can lead to enhanced Q by enabling homogeneous KO₂ distribution and high degrees of pore filling due to an enhanced surface area with the introduction of micropores and mesopores.

Figure 6C shows the discharge overpotentials, η_{dis} with O/C ratios of CP, CP_4 h, CP_12 h and CP_24 (left to right). It can be observed that the η_{dis} is decreasing with increasing O/C ratio at the three different current densities, with the most pronounced decrease from CP to CP_4 h. We attribute this to a significant increase in O-C=O groups, as the introduction of O-C=O groups was reported decrease in the discharge overpotentials in LOB, accordingly [26,40]. It is believed that the oxygen-containing functional groups and defects have a suitable adsorption energy for oxygen molecules [41], thus lowering the activation energy of the rate determining step and then subsequently enhancing the discharge voltage [26]. Transferred to the presented samples here, the reduction in the overpotential may also be caused the oxygen groups in a similar way.

4. Conclusions

In this work, the effect of the thermal pretreatment in air with three different pre-treatment times on the discharge performance of a commercially available carbon paper was studied. The modification in properties, i.e., in surface area, porosity and surface functionality, have been found to enhance the discharge capacity by enabling homogeneous KO₂ distribution and high degrees of pore filling. At the same time, the introduction of oxygen-containing functional surface groups and defects are considered causative for the observed reduction in discharge overpotentials. These findings display a promising way to further enhance the overall performance of KOB by the microstructural and functional design of carbon-based cathodes.

Supplementary Materials: The following supporting information can be downloaded at: <https://www.mdpi.com/article/10.3390/batteries10060192/s1>; Figure S1: SEM images of (a) CP, (b) CP_4 h, (c) CP_12 h and (d) CP_24 h at low magnification; Figure S2: (a) SEM overview images of carbon paper untreated and treated for 4 h, 12 h and 24 h with their respective EDS mappings of carbon (C_K, red) and oxygen (O_K, green), (b) Each mapping from (a) was evaluated by selecting 5 to 6 representative areas on the fibers. The resulting net intensities (includes background correction and peak deconvolution, scalebar given as counts) were plotted with the respective min/max deviations for each sample; Figure S3: Bright field TEM images of (a) CP and (b) CP_24 h; Figure S4: Photographs of contact angle measurements for (a) CP, (b) CP_4 h with DI water and (c) CP, (d) CP_4 h for DMSO; Figure S5: Raman spectra of (a) CP, (b) CP_4 h, (c) CP_12 h, and (d) CP_24 h; Figure S6: High resolution XPS spectra in the C 1s region for (a) CP, (b) CP_4 h, (c) CP_12 h and (d) CP_24 h; Figure S7: High resolution XPS spectra in the O 1s region for (a) CP, (b) CP_4 h, (c) CP_12 h and (d) CP_24 h;

Figure S8: Bode plots obtained via EIS for CP (black), CP_4 h (orange), CP_12 h (green) and CP_24 h (red); Figure S9: Cross-sectional SEM images of pristine CP (a), CP after discharge at $J = 0.1 \text{ mA/cm}^2$ (b) and $J = 1.0 \text{ mA/cm}^2$ (c), CP_12 h after discharge at $J = 0.1 \text{ mA/cm}^2$ (d) and $J = 1.0 \text{ mA/cm}^2$ (e), CP_24 h after discharge at $J = 0.1 \text{ mA/cm}^2$ (f) and $J = 1.0 \text{ mA/cm}^2$ (g); Table S1: All the quantitative values of various parameters of CP, CP_4 h, CP_12 h and CP_24 h

Author Contributions: Conceptualization, S.S., J.K. and U.S.; methodology, S.S.; validation, S.S.; investigation, S.S., M.N. and A.A.; resources, U.S.; data curation, S.S., A.A. and G.D.; writing—original draft preparation, S.S.; writing—review and editing, M.N. and U.S.; supervision, U.S.; project administration, M.N.; funding acquisition, U.S. All authors have read and agreed to the published version of the manuscript.

Funding: This research was funded by the Deutsche Forschungsgemeinschaft (DFG, German Research Foundation)—GRK 1856.

Data Availability Statement: The original contributions presented in the study are included in the article/Supplementary Materials, further inquiries can be directed to the corresponding authors.

Acknowledgments: We are grateful to K. Fries for TEM measurements, K. Turke, Anton Paar Germany GmbH for the gas adsorption–desorption measurements, and P. Pöllmann, Materials Chemistry, RWTH Aachen University for the assistance in XPS measurements.

Conflicts of Interest: The authors declare no conflicts of interest.

References

- Choi, N.S.; Chen, Z.; Freunberger, S.A.; Ji, X.; Sun, Y.K.; Amine, K.; Yushin, G.; Nazar, L.F.; Cho, J.; Bruce, P.G. Challenges facing lithium batteries and electrical double-layer capacitors. *Angew. Chem. Int. Ed. Engl.* **2012**, *51*, 9994–10024. [[CrossRef](#)]
- Girishkumar, G.; McCloskey, B.; Luntz, A.C.; Swanson, S.; Wilcke, W. Lithium–Air Battery: Promise and Challenges. *J. Phys. Chem. Lett.* **2010**, *1*, 2193–2203. [[CrossRef](#)]
- Ren, X.; Wu, Y. A low-overpotential potassium–oxygen battery based on potassium superoxide. *J. Am. Chem. Soc.* **2013**, *135*, 2923–2926. [[CrossRef](#)]
- Aurbach, D.; McCloskey, B.D.; Nazar, L.F.; Bruce, P.G. Advances in understanding mechanisms underpinning lithium–Air batteries. *Nat. Energy* **2016**, *1*, 16128. [[CrossRef](#)]
- Yao, X.; Dong, Q.; Cheng, Q.; Wang, D. Why Do Lithium–Oxygen Batteries Fail: Parasitic Chemical Reactions and Their Synergistic Effect. *Angew. Chem. Int. Ed.* **2016**, *55*, 11344–11353. [[CrossRef](#)]
- Mahne, N.; Schafzahl, B.; Leypold, C.; Leypold, M.; Grumm, S.; Leitgeb, A.; Strohmeier, Gernot, A.; Wilkening, M.; Fontaine, O.; et al. Singlet oxygen generation as a major cause for parasitic reactions during cycling of aprotic lithium–oxygen batteries. *Nat. Energy* **2017**, *2*, 17036. [[CrossRef](#)]
- Mourad, E.; Petit, Y.K.; Spezia, R.; Samojlov, A.; Summa, F.F.; Prehal, C.; Leypold, C.; Mahne, N.; Slugovc, C.; Fontaine, O.; et al. Singlet oxygen from cation driven superoxide disproportionation and consequences for aprotic metal–O₂ batteries. *Energy Environ. Sci.* **2019**, *12*, 2559–2568. [[CrossRef](#)]
- Houchins, G.; Pande, V.; Viswanathan, V. Mechanism for Singlet Oxygen Production in Li-Ion and Metal–Air Batteries. *ACS Energy Lett.* **2020**, *5*, 1893–1899. [[CrossRef](#)]
- Reinsberg, P.H.; Koellisch, A.; Baltruschat, H. On the importance of ion pair formation and the effect of water in potassium–Oxygen batteries. *Electrochim. Acta* **2019**, *313*, 223–234. [[CrossRef](#)]
- Xiao, N.; Rooney, R.T.; Gewirth, A.A.; Wu, Y. The Long-Term Stability of KO₂ in K–O₂ Batteries. *Angew. Chem. Int. Ed.* **2018**, *57*, 1227–1231. [[CrossRef](#)]
- Qin, L.; Schkeryantz, L.; Zheng, J.; Xiao, N.; Wu, Y. Superoxide-Based K–O₂ Batteries: Highly Reversible Oxygen Redox Solves Challenges in Air Electrodes. *J. Am. Chem. Soc.* **2020**, *142*, 11629–11640. [[CrossRef](#)]
- Xiao, N.; Ren, X.; McCulloch, W.D.; Gourdin, G.; Wu, Y. Potassium Superoxide: A Unique Alternative for Metal–Air Batteries. *Acc. Chem. Res.* **2018**, *51*, 2335–2343. [[CrossRef](#)]
- Park, J.; Hwang, J.-Y.; Kwak, W.-J. Potassium–Oxygen Batteries: Significance, Challenges, and Prospects. *J. Phys. Chem. Lett.* **2020**, *11*, 7849–7856. [[CrossRef](#)]
- Ren, X.; Lau, K.C.; Yu, M.; Bi, X.; Kreidler, E.; Curtiss, L.A.; Wu, Y. Understanding Side Reactions in K–O₂ Batteries for Improved Cycle Life. *ACS Appl. Mater. Interfaces* **2014**, *6*, 19299–19307. [[CrossRef](#)]
- Yu, W.; Lau, K.C.; Lei, Y.; Liu, R.; Qin, L.; Yang, W.; Li, B.; Curtiss, L.A.; Zhai, D.; Kang, F. Dendrite-Free Potassium–Oxygen Battery Based on a Liquid Alloy Anode. *ACS Appl. Mater. Interfaces* **2017**, *9*, 31871–31878. [[CrossRef](#)]
- McCulloch, W.D.; Ren, X.; Yu, M.; Huang, Z.; Wu, Y. Potassium–Ion Oxygen Battery Based on a High Capacity Antimony Anode. *ACS Appl. Mater. Interfaces* **2015**, *7*, 26158–26166. [[CrossRef](#)]
- Eftekhari, A.; Jian, Z.; Ji, X. Potassium Secondary Batteries. *ACS Appl. Mater. Interfaces* **2017**, *9*, 4404–4419. [[CrossRef](#)]

18. Xiao, N.; Gourdin, G.; Wu, Y. Simultaneous Stabilization of Potassium Metal and Superoxide in K–O₂ Batteries on the Basis of Electrolyte Reactivity. *Angew. Chem. Int. Ed.* **2018**, *57*, 10864–10867. [[CrossRef](#)]
19. Gilmore, P.; Sundaresan, V.B. A Functionally Graded Cathode Architecture for Extending the Cycle-Life of Potassium–Oxygen Batteries. *Batter. Supercaps* **2019**, *2*, 662. [[CrossRef](#)]
20. Cong, G.; Wang, W.; Lai, N.-C.; Liang, Z.; Lu, Y.-C. A high-rate and long-life organic–oxygen battery. *Nat. Mater.* **2019**, *18*, 390–396. [[CrossRef](#)]
21. Küpper, J.; Jakobi, S.; Simon, U. PTFE Enhances Discharge Performance of Carbon Cathodes in Potassium–Oxygen Batteries. *Batter. Supercaps* **2021**, *4*, 1620–1626. [[CrossRef](#)]
22. Küpper, J.; Simon, U. The effects of oxygen pressure on the discharge performance of potassium–Oxygen batteries. *Sustain. Energy Fuels* **2022**, *6*, 1992–2000. [[CrossRef](#)]
23. Küpper, J.; Li, X.; Simon, U. A Model of the Potassium–Oxygen Battery and its Application in Cathode Design. *J. Electrochem. Soc.* **2022**, *169*, 060539. [[CrossRef](#)]
24. Singh, A.; Yasri, N.; Karan, K.; Roberts, E. Electrocatalytic Activity of Functionalized Carbon Paper Electrodes and Their Correlation to the Fermi Level Derived from Raman Spectra. *ACS Appl. Energy Mater.* **2019**, *2*, 2324–2336. [[CrossRef](#)]
25. Yue, Z.R.; Jiang, W.; Wang, L.; Gardner, S.D.; Pittman, C.U. Surface characterization of electrochemically oxidized carbon fibers. *Carbon* **1999**, *37*, 1785–1796. [[CrossRef](#)]
26. Qian, Z.; Sun, B.; Du, L.; Lou, S.; Du, C.; Zuo, P.; Ma, Y.; Cheng, X.; Gao, Y.; Yin, G. Insights into the role of oxygen functional groups and defects in the rechargeable nonaqueous Li–O₂ batteries. *Electrochim. Acta* **2018**, *292*, 838–845. [[CrossRef](#)]
27. Li, Z.; Deng, L.; Kinloch, I.A.; Young, R.J. Raman spectroscopy of carbon materials and their composites: Graphene, nanotubes and fibres. *Prog. Mater. Sci.* **2023**, *135*, 101089. [[CrossRef](#)]
28. Stankovich, S.; Dikin, D.A.; Piner, R.D.; Kohlhaas, K.A.; Kleinhammes, A.; Jia, Y.; Wu, Y.; Nguyen, S.T.; Ruoff, R.S. Synthesis of graphene-based nanosheets via chemical reduction of exfoliated graphite oxide. *Carbon* **2007**, *45*, 1558–1565. [[CrossRef](#)]
29. Kwon, S.; Suharto, Y.; Kim, K.J. Facile preparation of an oxygen-functionalized carbon felt electrode to improve VO²⁺/VO₂⁺ redox chemistry in vanadium redox flow batteries. *J. Ind. Eng. Chem.* **2021**, *98*, 231–236. [[CrossRef](#)]
30. Liu, T.; Li, X.; Xu, C.; Zhang, H. Activated Carbon Fiber Paper Based Electrodes with High Electrocatalytic Activity for Vanadium Flow Batteries with Improved Power Density. *ACS Appl. Mater. Interfaces* **2017**, *9*, 4626–4633. [[CrossRef](#)]
31. Ulaganathan, M.; Aravindan, V.; Yan, Q.; Madhavi, S.; Skyllas-Kazacos, M.; Lim, T.M. Recent Advancements in All-Vanadium Redox Flow Batteries. *Adv. Mater. Interfaces* **2016**, *3*, 1500309. [[CrossRef](#)]
32. Zeng, L.; Zhao, T.; Wei, L. Revealing the Performance Enhancement of Oxygenated Carbonaceous Materials for Vanadium Redox Flow Batteries: Functional Groups or Specific Surface Area? *Adv. Sustain. Syst.* **2018**, *2*, 1700148. [[CrossRef](#)]
33. Yang, S.; Li, L.; Xiao, T.; Zheng, D.; Zhang, Y. Role of surface chemistry in modified ACF (activated carbon fiber)-catalyzed peroxyomonosulfate oxidation. *Appl. Surf. Sci.* **2016**, *383*, 142–150. [[CrossRef](#)]
34. Pacheco, F.G.; Cotta, A.A.C.; Gorgulho, H.F.; Santos, A.P.; Macedo, W.A.A.; Furtado, C.A. Comparative temporal analysis of multiwalled carbon nanotube oxidation reactions: Evaluating chemical modifications on true nanotube surface. *Appl. Surf. Sci.* **2015**, *357*, 1015–1023. [[CrossRef](#)]
35. Knudsen, K.B.; Nichols, J.E.; Vegge, T.; Luntz, A.C.; McCloskey, B.D.; Hjelm, J. An Electrochemical Impedance Study of the Capacity Limitations in Na–O₂ Cells. *J. Phys. Chem. C* **2016**, *120*, 10799–10805. [[CrossRef](#)]
36. Wang, F.; Li, X. Effects of the Electrode Wettability on the Deep Discharge Capacity of Li–O₂ Batteries. *ACS Omega* **2018**, *3*, 6006–6012. [[CrossRef](#)]
37. Riaz, A.; Jung, K.-N.; Lee, J.-W. A Mini-Review on Non-Aqueous Lithium–Oxygen Batteries—Electrochemistry and Cathode Materials. *J. Electrochem. Sci. Technol.* **2015**, *6*, 50–58. [[CrossRef](#)]
38. Kim, M.; Yoo, E.; Ahn, W.-S.; Shim, S.E. Controlling porosity of porous carbon cathode for lithium oxygen batteries: Influence of micro and meso porosity. *J. Power Sources* **2018**, *389*, 20–27. [[CrossRef](#)]
39. Zhao, T.; Yao, Y.; Yuan, Y.; Wang, M.; Wu, F.; Amine, K.; Lu, J. A universal method to fabricating porous carbon for Li–O₂ battery. *Nano Energy* **2021**, *82*, 105782. [[CrossRef](#)]
40. Huang, S.; Fan, W.; Guo, X.; Meng, F.; Liu, X. Positive role of surface defects on carbon nanotube cathodes in overpotential and capacity retention of rechargeable lithium–oxygen batteries. *ACS Appl. Mater. Interfaces* **2014**, *6*, 21567–21575. [[CrossRef](#)]
41. Xiao, J.; Mei, D.; Li, X.; Xu, W.; Wang, D.; Graff, G.L.; Bennett, W.D.; Nie, Z.; Saraf, L.V.; Aksay, I.A.; et al. Hierarchically Porous Graphene as a Lithium–Air Battery Electrode. *Nano Lett.* **2011**, *11*, 5071–5078. [[CrossRef](#)]

Disclaimer/Publisher’s Note: The statements, opinions and data contained in all publications are solely those of the individual author(s) and contributor(s) and not of MDPI and/or the editor(s). MDPI and/or the editor(s) disclaim responsibility for any injury to people or property resulting from any ideas, methods, instructions or products referred to in the content.